remote sensing

MDPI

Article

Evolution Patterns and Dominant Factors of Soil Salinization in the Yellow River Delta Based on Long-Time-Series and Similar Phenological-Fusion Images

Bing Guo [1], Mei Xu [1] and Rui Zhang [2,*]

[1] School of Civil Engineering and Geomatics, Shandong University of Technology, Zibo 255000, China; guobing@sdut.edu.cn (B.G.); 22407010008@stumail.sdut.edu.cn (M.X.)
[2] Key Laboratory of Remote Sensing of Gansu Province, Heihe Remote Sensing Experimental Research Station, Northwest Institute of Eco-Environment and Resources, Chinese Academy of Sciences, Lanzhou 730000, China
* Correspondence: zhangrui@radi.ac.cn

Abstract: Previous studies were mostly conducted based on sparse time series and different phenological images, which often ignored the dramatic changes in salinization evolution throughout the year. Based on Landsat and moderate-resolution-imaging spectroradiometer (MODIS) images from 2000 to 2020, this study applied the Enhanced Spatial and Temporal Adaptive Reflectance Fusion Model (ESTARFM) algorithm to obtain similar phenological images for the month of April for the past 20 years. Based on the random forest algorithm, the surface parameters of the salinization were optimized, and the feature space index models were constructed. Combined with the measured ground data, the optimal monitoring index model of salinization was determined, and then the spatiotemporal evolution patterns of salinization and its driving mechanisms in the Yellow River Delta were revealed. The main conclusions were as follows: (1) The derived long-time-series and similar phenological-fusion images enable us to reveal the patterns of change in the dramatic salinization in the year that we examined using the ESTARFM algorithm. (2) The NDSI-TGDVI feature space salinization monitoring index model based on point-to-point mode had the highest accuracy of 0.92. (3) From 2000 to 2020, the soil salinization in the Yellow River Delta showed an aggravating trend. The average value of salinization during the past 20 years was 0.65, which is categorized as severe salinization. The degree of salinization gradually decreased from the northeastern coastal area to the southwestern inland area. (4) The dominant factors affecting soil salinization in different historical periods varied. The research results could provide support for decision-making regarding the precise prevention and control of salinization in the Yellow River Delta.

Keywords: soil salinization; ESTARFM; change process; Yellow River Delta; dominant factors

check for updates

Citation: Guo, B.; Xu, M.; Zhang, R. Evolution Patterns and Dominant Factors of Soil Salinization in the Yellow River Delta Based on Long-Time-Series and Similar Phenological-Fusion Images. *Remote Sens.* **2024**, *16*, 3332. https://doi.org/10.3390/rs16173332

Academic Editors: Dominique Arrouays and Jeroen Meersmans

Received: 26 June 2024
Revised: 14 August 2024
Accepted: 6 September 2024
Published: 8 September 2024

Copyright: © 2024 by the authors. Licensee MDPI, Basel, Switzerland. This article is an open access article distributed under the terms and conditions of the Creative Commons Attribution (CC BY) license (https://creativecommons.org/licenses/by/4.0/).

1. Introduction

Aggravated global soil salinization, which influences the quality of soil and greatly constrains crop production, has become an obvious global eco-environmental problem. Over 1 billion hectares of soil are suffering from salinization. Recently, soil salinization has become a significant ecological and environmental issue, both domestically and internationally. Due to the influences of natural and human factors, salinized soil has been widely distributed in arid, semi-arid, and semi-humid areas of northern China, especially in coastal areas. Since the 1970s, the Yellow River Delta has experienced an imbalance in land flooding due to reduced water and sediment levels and seawater backflow [1]. In recent years, the problem of salinization in the Yellow River Delta has been particularly prominent. Severe salinization has led to soil degradation and compaction, and reduced land productivity has limited crop growth, leading to enormous pressure on arable land resources, exacerbating the deterioration of the ecological environment and thus restricting

the sustainable development of society and the economy and endangering human health [2]. Over 70% of the land is saline soil to varying degrees, posing a serious threat to regional food security, the layout of ecological protection red lines, and the sustainable development of agriculture. In 2019, at a symposium on advancing ecological protection and high-quality development in the Yellow River Basin, General Secretary Xi Jinping emphasized the need to create conditions for steadily advancing the restoration of wetlands and floodplains and strengthening the protection of biological species resources in salt marshes, tidal flats, and estuarine shallow seas. This underscores the importance of the environmental protection of wetlands in the Yellow River Delta from a national strategic perspective. Related studies show that in recent decades, soil salinization in the Yellow River Delta has been exacerbated by natural factors (temperature, precipitation, sunshine hours, altitude, slope, aspect, etc.) and human activities (population density, gross domestic product (GDP), etc.) [3]. It is imperative to explore the spatiotemporal evolution characteristics and patterns of the occurrence, development, and reversal of salinization in the modern Yellow River Delta in depth. These issues are caused by natural factors, human activities, or a combination of both, as well as their direction of action (promotion or inhibition) and contribution rate. Therefore, dynamic and regular monitoring of soil salinization requires knowledge of when, where, and how salinization occurs, which is crucial for the proper management of soil and water resources.

The current monitoring methods for salinization can be divided into the field positioning observation method and the remote sensing technology extraction method [4–6]. Although traditional field observation methods achieved high accuracy, they were time-consuming, labor intensive, and limited to a small scale [7–10]. With the continuous launches of Earth observation satellites, remote sensing has become the main approach for dynamically monitoring salinization at large scales [11,12]. Domestic and international scholars have adopted image classification, the comprehensive index method, and multiple regression analysis to qualitatively or quantitatively extract salinization information based on remote sensing images, which have achieved a series of better results [13–16]. Kumar et al. [17] assessed soil salinization by mapping the salinity and electrical conductivity of saturation extracts and utilizing spectral signatures for estimating soil salinity. Wang et al. [18] proposed a framework to quantitatively estimate the global content of salt in soil in five climate regions at 10 m by integrating Sentinel-1/2 images, climate data, parent material, terrain data, and machine learning. However, while image classification methods have certain advantages in defining the scope of salinization, they cannot obtain internal spatial variation information. The comprehensive index method and multiple regression analysis method are able to consider the influences of multiple factors on the salinization process, but they cannot consider the interactions between factors and the nonlinear characteristics of their impacts on the salinization process [19,20]. In recent years, many scholars have attempted to introduce the soil salinity index [21], humidity index [22,23], surface albedo [24], vegetation index [25,26], surface temperature [27,28], and iron oxide index [29,30] based on the feature space method for remote sensing inversion of soil salinization information and have achieved good results. However, most of the above studies constructed a single linear model or distance model in a two-dimensional feature space, ignoring the nonlinear coupling effects between parameters. Guo et al. [31] utilized five typical surface parameters to construct ten different feature spaces and then proposed two different kinds of monitoring models (the point-to-point model and the point-to-line model) of soil salinization. Meanwhile, with the increase in available salinization characterization parameters (indicating different biotic–abiotic factors), selecting the most suitable parameters based on regional environmental characteristics for feature space construction has become the primary issue that urgently needs to be addressed in the aforementioned research. In recent years, relevant studies found that the random forest algorithm has significant advantages in determining the optimal characterized parameters. This algorithm can automatically distinguish the importance of variables and determine dependency relationships between variables [32–34]. Therefore, the introduction of the

random forest algorithm to determine the optimal characterization parameter quantum set for salinization in the Yellow River Delta and the construction of a nonlinear feature space monitoring model for salinization are both worthy of in-depth research.

The Yellow River Delta is located at the junction of the atmosphere, ocean, river, and land, with a typical multiple ecological interface and fragmented surface landscape pattern (especially wetlands), which causes its intense environmental gradient and rapid salinization succession process [35]. Some scholars conducted a series of studies on the inversion methods and spatiotemporal variation patterns of salinization in the Yellow River Delta based on multi-source remote sensing data and achieved a range of results [27,36]. However, the above studies were mostly based on single-temporal, dual-temporal, or sparse temporal images. Although they could reveal the overall trend of and changes in salinization status to some extent, they often overlooked the drastic changes in the salinization evaluation process within a year.

Due to the low temporal resolution of satellites with high-spatial-resolution image acquisition capabilities, the contradictions between spatial and temporal resolutions in remote sensing images have become an unavoidable practical problem for achieving intensive and long-term monitoring of salinization [37–39]. At present, compared with hardware solutions (launching new Earth observation satellites), spatiotemporal-data-fusion technology has become an important low-cost, efficient, and feasible means of obtaining medium-to-high-spatiotemporal-resolution datasets. Recently, domestic and international scholars have conducted extensive research on spatiotemporal-fusion algorithms (the Spatial and Temporal Adaptive Reflectance Fusion Model (STARFM), the ESTARFM, the LIU model, the Spatial and Temporal Adaptive Reflectance Fusion Model (STDFAT), and the Spatial Temporal Data Fusion Approach (STDFA) model) based on multi-source satellite data such as Landsat (high spatial–low temporal), MODIS (low spatial–high temporal), and AVHRR (low spatial–high temporal). Among them, the ESTARFM has shown good applicability in target study areas with complex and fragmented surface cover types or terrain conditions [40–44]. In this study, the ESTARFM was applied to obtain high-spatiotemporal-resolution and similar phenological-fusion images, thereby achieving long-term remote sensing monitoring of salinization in the Yellow River Delta.

The objective and novelty of this paper is the revelation of the spatial and temporal change patterns and their dominant factors based on similar phenological images. Therefore, based on the Landsat and MODIS datasets from 2000 to 2020, spatiotemporal-fusion algorithms were applied to obtain similar phenological-fusion images for the month of April for the past 20 years. Utilizing the random forest algorithm, the reverse surface parameters were optimized, and the feature space index models were constructed. The optimal salinization index model was determined by combining observed field data, and then the spatiotemporal evolution pattern and driving mechanism of salinization in the Yellow River Delta were comprehensively examined. This paper clarifies which patterns are caused by natural factors and which are caused by human activities and determines their direction of action and contribution rate. It highlights the key areas for preventing and controlling salinization, which can directly provide theoretical support for decision-making regarding the implementation of efficient and accurate salinization prevention and control measures in the Yellow River Delta and even at the national level.

2. Data Source and Methods

2.1. Study Area

The Yellow River Delta (Figure 1) is located in the northern part of the Shandong Province (37°20′–38°12′N, 118°07′–119°10′E), with Lijin County as the vertex, north of the Tuhai River Estuary and south of the Xiaoqing River Estuary. It is a fan-shaped, triangular area mainly within the territory of Dongying City. The name refers to the alluvial plain formed by sedimentation in the Bohai Depression of the Yellow River Basin, covering an area of approximately 7033.41 km^2, which is a typical area of coastal saline soil in the Shandong Province. The study region is situated in a warm-temperate, semi-humid, continental

monsoon climate zone, which is characterized by hot and rainy summers and cold and dry winters, with an average precipitation of about 600–800 mm [26]. The seasons alternate distinctly, with significant temperature and humidity differences, while the evaporation rate far exceeds the precipitation, with an annual evaporation-to-precipitation ratio of about 3.5:1, providing favorable conditions for the upward movement of salts [38]. The terrain is flat, gradually decreasing from southwest to northeast, with vast tidal flats [20]. The elevation is around 11 m in the southwest, while it is less than 1 m at the lowest point in the northeast. The groundwater has high mineralization levels and varying depths, with the predominant soil types being saline soil and tidal soil [22]. Due to distinct and intricate land hydrological features, interactions between different media result in the geographical environment having a high degree of sensitivity to external changes. Additionally, the low-lying coastal terrain makes the area prone to phenomena such as seawater intrusion. As a result, salinization levels are relatively high in coastal regions. In recent decades, the evolution pattern of salinization in the Yellow River Delta has undergone changes under the combined effects of climate change, human activities, and ocean dynamics.

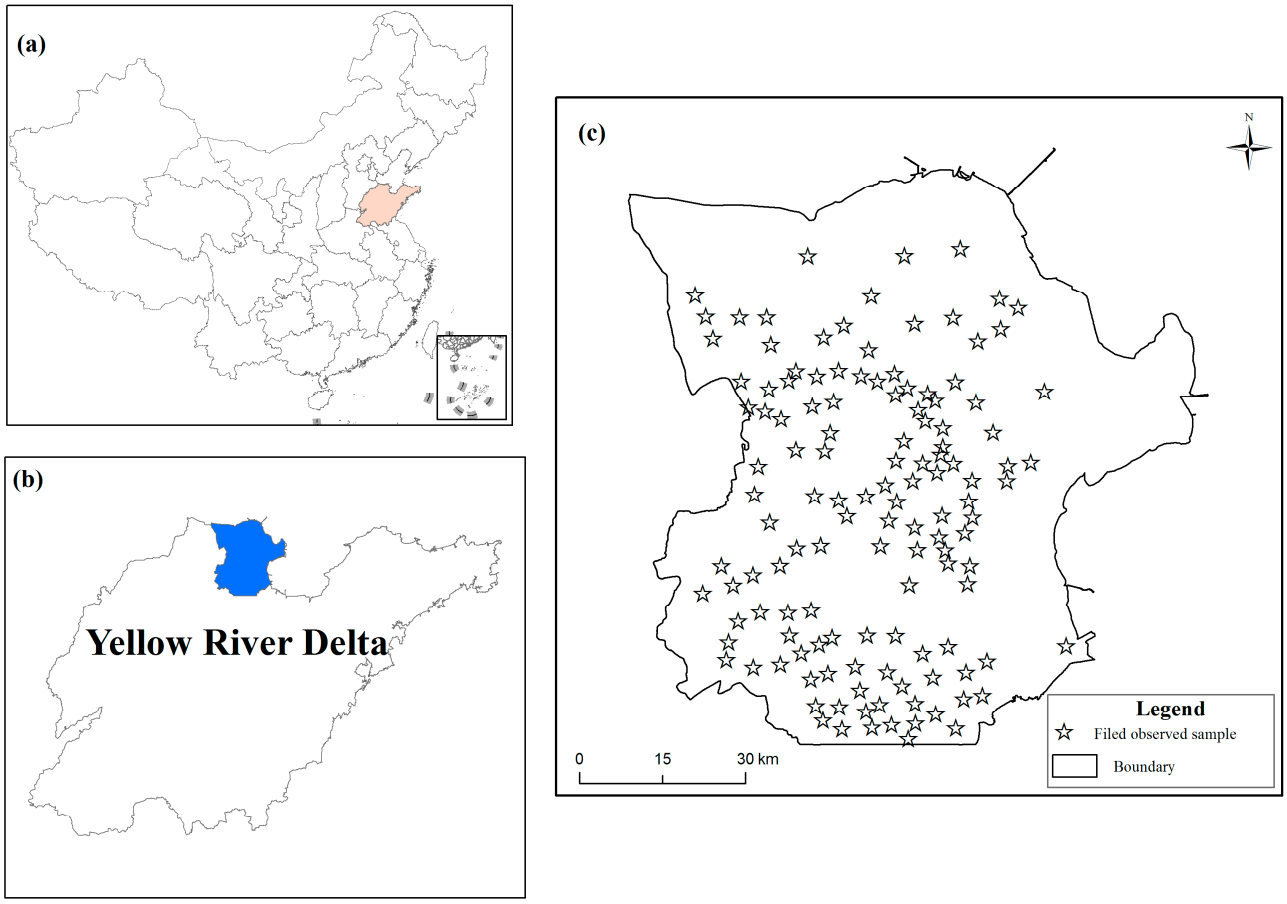


Figure 1. The location of the study area and the distribution of the observed samples from the field. (**a**) the location of the study area in China; (**b**) the location of the study area in Shandong Province; (**c**) the location of the study area.

2.2. Data Source and Preprocessing

2.2.1. Remote Sensing Images

The Landsat image datasets with cloud cover <10% from 2000 to 2020 came from the geospatial data cloud platform of the Computer Network Information Center of the Chinese Academy of Sciences (http://www.gscloud.cn/, accessed on 8 January 2024) and the United States Geological Survey (http://glovis.usgs.gov/, accessed on 5 January 2024). The 8-day MOD09A1 products with a spatial resolution of 500 m were downloaded from

http://www.nasa.gov (accessed on 7 January 2024). The time of data acquisition for the MODIS product and Landsat images must be in the same month. Using ENVI 5.3, the radiometric calibration, atmospheric correction, and other preprocessing steps for the acquired Landsat data were performed. The MODIS Reprojection Tool (MRT) was adopted to project and resample the MOD09A1 data to a 30 m resolution. We then cropped the data to the same extent for fusion (Appendix A Table A1).

2.2.2. Field Measurement Data

In April, the surface salinization in the Yellow River Delta remained stable. During the sampling process, soil samples were taken from a 0–20 cm depth, with 4–5 collection points arranged in a 5-point plum-blossom pattern. After thorough mixing, an appropriate amount of soil was placed into sample bags. Based on the differences in soil salinization degree, surface morphology, and microtopography in the Yellow River Delta, 146 measurement units (30 m × 30 m) were set up, with global positioning system (GPS) coordinates and surrounding environmental information being recorded. We air-dried and crushed the collected soil samples naturally, removed other invading bodies, sieved through a 1 mm sieve, and mixed evenly. We then used the quartering method to sample 200 g and prepare a 1:5 soil/water ratio leaching solution for soil salt determination. Finally, we took the average of each of the 5 soil sampling points as the observation value of the soil measurement unit. The mean, minimum, and maximum salt content of these samples were 0.15%, 0, and 2.48%, respectively.

2.2.3. Natural-Factor Data and Socio-Economic Factors

(1) The land-use data from 2000 to 2020 were obtained from the Resource and Environmental Science and Data Center of the Chinese Academy of Sciences (http://www.resdc.cn/, accessed on 10 January 2024), with a spatial resolution of 30 m.

(2) The DEM data were sourced from the Geographic National Conditions Monitoring Cloud Platform (http://www.dsac.cn/, accessed on 15 January 2024), with a spatial resolution of 30 m. Using the ArcGIS software, the slope and aspect data were extracted using the slope and aspect tools based on the DEM data l, respectively.

(3) The dataset for the soil bulk density and effective soil moisture content was sourced from the National Qinghai Tibet Plateau Science Data Center (https://data.tpdc.ac.cn/, accessed on 8 January 2024). Its projection was WGS84, and the data format was a grid raster. The unit for the available water content in soil was percentage (%), and the unit for the soil bulk density was kg/cubic meter.

(4) The meteorological data, such as rainfall and temperature, from 2000 to 2020 were all obtained from the China Meteorological Data Sharing Network (http://data.cma.cn/, accessed on 12 January 2024). Using the ArcGIS geostatistical guide tool, we performed Kriging interpolation on the meteorological station data, cropped the interpolated raster data, and obtained the meteorological data for the Yellow River Delta.

(5) The population and GDP data from 2000 to 2020 were sourced from the China Population/GDP Spatial Distribution Kilometer Grid Dataset of the Resource and Environmental Science and Data Center of the Chinese Academy of Sciences (http://www.resdc.cn/, accessed on 8 January 2024).

2.3. Research Methods

The flowchart of the entire paper is presented in Figure 2.

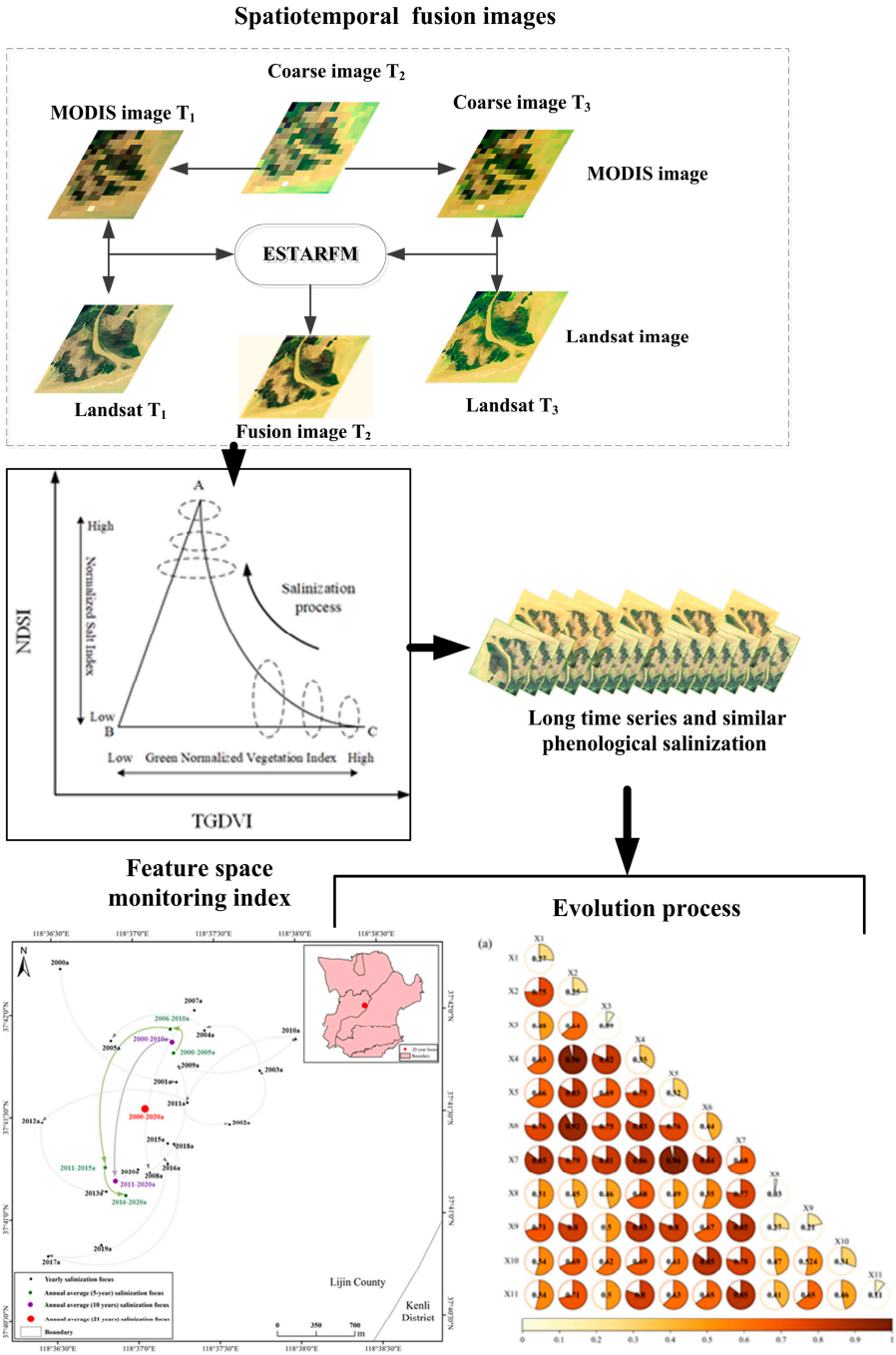


Figure 2. The flowchart of the entire paper.

2.3.1. Spatiotemporal-Fusion Algorithm

The principle of the ESTARFM [45] is to blend multi-source data using correlation while minimizing system biases. The algorithm was used based on a low-resolution image of a predicted date and two pairs of low-/high-resolution images to construct high-resolution temporal and spatial data for the predicted date. This model showed good applicability in target study areas with complex and fragmented surface cover types or terrain conditions. The specific algorithm is as follows:

$$F(x_i, y_i, t_k, B) = a \times C(x_i, y_i, t_k, B) + b \quad (1)$$

where F and C represent the reflectance of high-resolution pixels and low-resolution pixels, respectively; (x_i, y_i) represent the given pixel positions of high-resolution and low-resolution

images; t_k is the date of data acquisition; and a and b are the coefficients of the linear regression model for the relative calibration of low-resolution and high-resolution reflectance.

2.3.2. Random Forest Algorithm

Random forest [46], proposed by Leo Breiman and Addle Cutler in 2001, is a machine learning algorithm based on ensemble learning principles. It can effectively estimate and handle missing values to ensure model accuracy, utilizes decision trees as the fundamental building blocks, and ranks the importance of feature variables. This study was conducted based on the error of the corresponding out-of-bag data used by each decision tree in a random forest to represent the importance of the feature variable, denoted as $errOOB_1$. Noise interference was randomly added to the feature X of all out-of-bag data samples, and the error was calculated, denoted as $errOOB_2$. Finally, the importance X of the feature variable was calculated. The calculation formula for importance is as follows:

$$X = \frac{1}{N}\sum_{i=1}^{N}(\mathrm{errOOB}_2 - \mathrm{errOOB}_1) \quad (2)$$

In this formula, N is the number of decision trees, errOOB_1 is the out-of-bag error of the decision tree, and errOOB_2 is the out-of-bag error calculated based on new values. The larger X is, the more important the feature variable is.

2.3.3. Feature Space Model

The feature space method has been widely used in fields such as salinization monitoring, drought monitoring, rocky desertification monitoring, and water retrieval. In recent years, many scholars have achieved good results in constructing relevant salinization models based on the feature space method for salinization monitoring. Therefore, this study proposed a monitoring index based on the feature space model to monitor the salinization process in the Yellow River Delta. Taking TGDVI-NDSI and EDVI-Albedo as examples (Figure 3), the distance from any point in the feature space of TGDVI-NDSI to (1,0) could represent the degree of salinization. The smaller the distance, the greater the degree of salinization. The distance from any point in the feature space of EDVI-Albedo to L represents the degree of salinization, with closer proximity indicating more severe salinization.

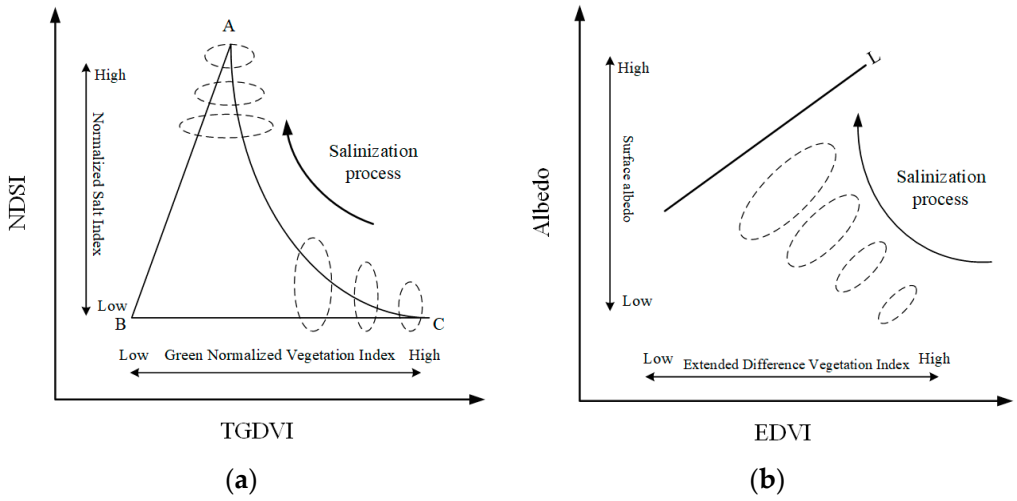


Figure 3. Principle of feature space method: (**a**) TGDVI-NDSI; (**b**) EDVI-Albedo.

2.3.4. Geographical Detector

Geographical detector has been widely applied in various fields such as land use, public health, regional planning, and remote sensing [47]. The core idea is to detect the consistency between the dependent and independent variables in the spatial distribution

pattern through spatial heterogeneity. Based on this measure, the explanatory power of the independent variable to the dependent variable, i.e., the q value, can be obtained. By combining GIS spatial superposition and theoretical assumptions, the influence of different combinations of two factors on the dependent variable after superposition is obtained to determine whether there is any interaction between the two factors and to obtain information on the strength, direction, and linearity or nonlinearity of the interaction. The question is to what extent the detection factor X explains the spatial differentiation of the attribute factor Y, and the expression to determine this is as follows:

$$q = 1 - \frac{\sum_{h=1}^{L} N_h \sigma_h^2}{N\sigma^2} = 1 - \frac{\mathrm{SSW}}{\mathrm{SST}} \tag{3}$$

$$\mathrm{SSW} = \sum_{h=1}^{L} N_h \sigma_h^2, \mathrm{SST} = n\sigma^2 \tag{4}$$

In this formula, $q \in [0, 1]$ and the larger q represent the stronger explanatory power of the driving factor X on Y; h is the stratification or classification of the variable Y or factor X; N_h is the number of units in the h layer; N is the unit number for the entire region; σ_h^2 is the variance of the h layer; σ^2 is the variance of the Y value for the entire region; SSW is the sum of intralayer variances; and SST is the total variance of the entire region.

The types of interactions between two independent variables and the dependent variable are shown in Figure 4.

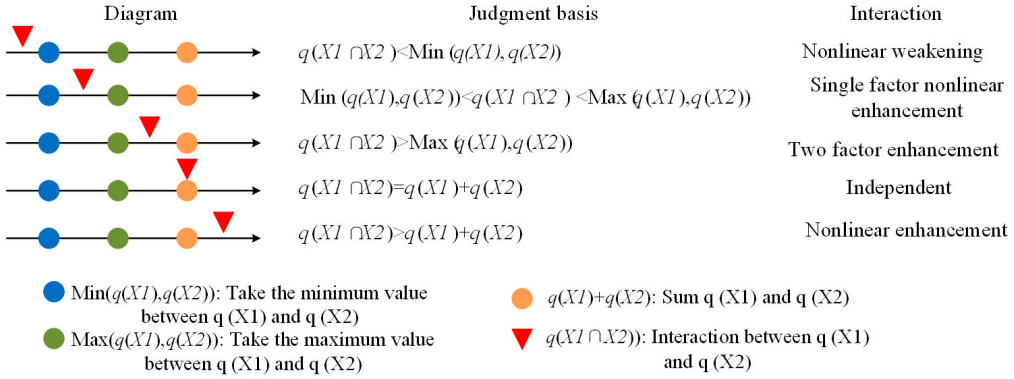


Figure 4. Types of interactive dominant factors affecting salinization changes.

3. Results

3.1. Construction of High-Spatiotemporal-Resolution Fusion Dataset Based on ESTARFM

This study used the image from 15 April 2001 as the baseline image and conducted fusion experiments on two sets of images from March and July 2001 (Figure 5). The visual interpretation of the fusion results (Figure 5b) and the actual images (Figure 5c) showed very high consistency. In the enlarged area of Figure 5d–f, it can be seen that the fusion results accurately depict the boundaries and positions between different areas of farmland and clearly reproduce the detailed information of real images, such as the textural structure and land information. The correlation analysis showed that the two images (Figure 5b,c) had a higher linear correlation, with a correlation coefficient of 0.8677 (Figure 6). Therefore, the fusion results of the ESTARFM algorithm reflected the spectral information of the actual Landsat images better, and this fusion model provided a suitable model for subsequent research on soil salinization, which was consistent overall with the research results of Yang et al. [48]. At the same time, the relevant evaluation indicators for image fusion quality were calculated using MATLAB, including the correlation coefficient R^2 (0.89), peak signal-to-noise ratio (PSNR) (77.56), information entropy (ENTROPY) (6.22), structural

similarity index (SSIM) (0.999), and average gradient (0.00386). Overall, they indicated that the ESTARFM had good applicability.

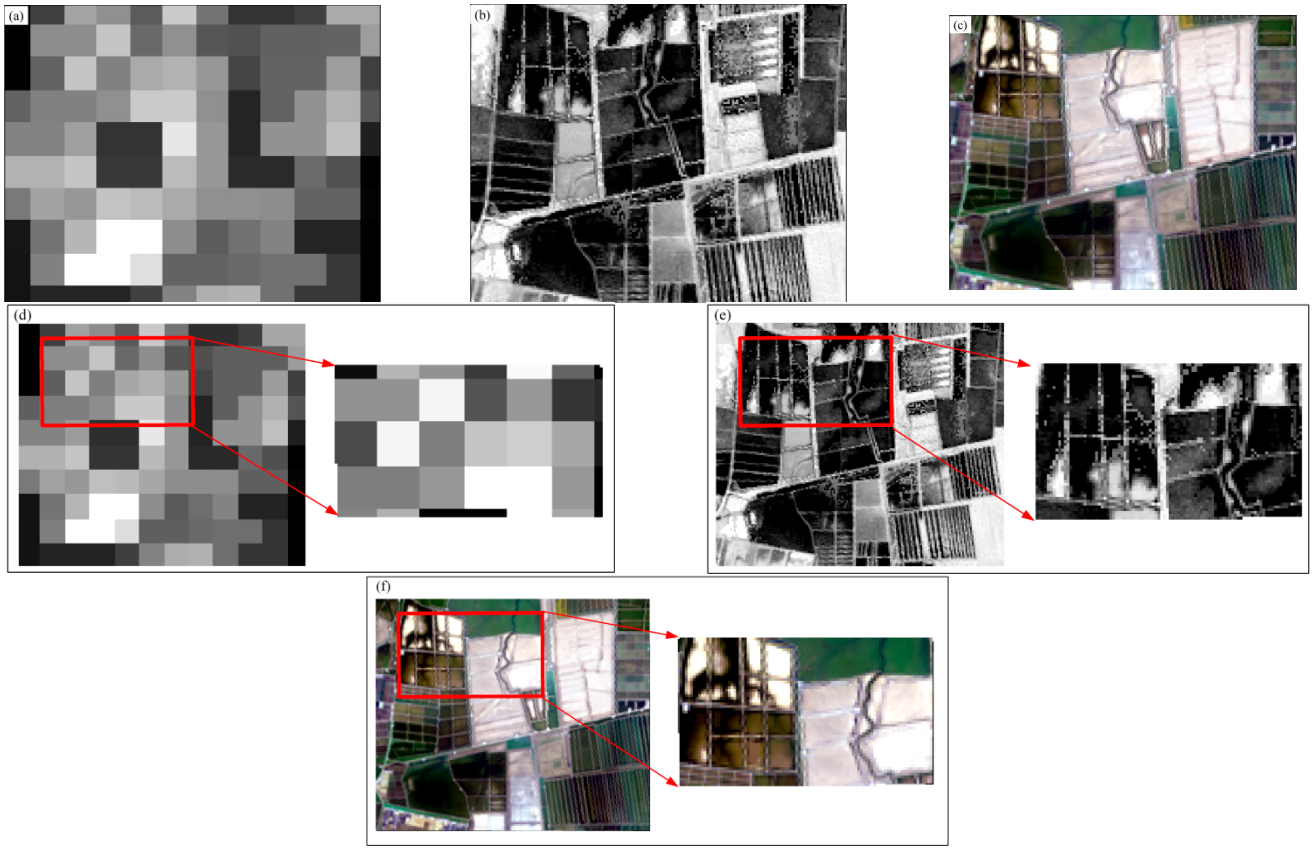


Figure 5. Comparison details of ESTARFM fusion results: (**a**) coarse-resolution image; (**b**) fusion image; (**c**) actual image; (**d**) enlarged area from coarse-resolution image; (**e**) enlarged area from fine-resolution image; and (**f**) enlarged area from actual-resolution image.

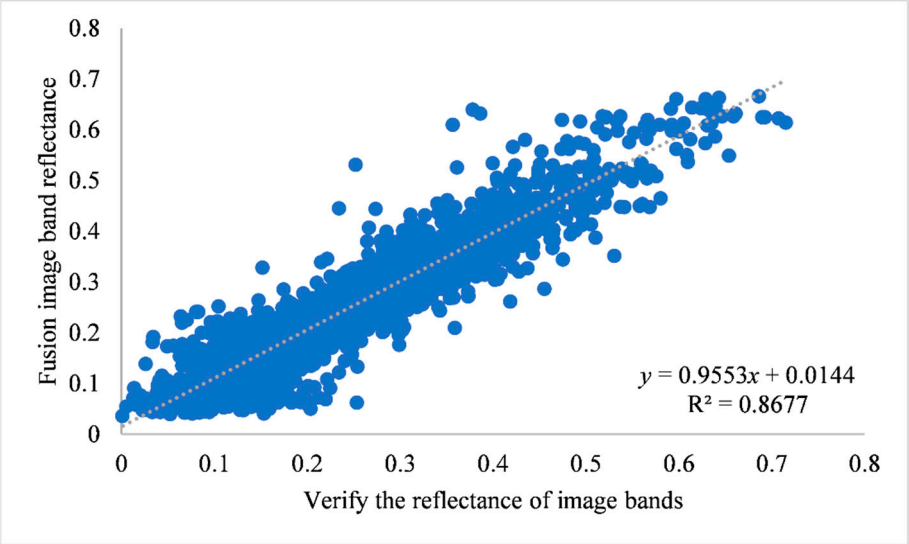


Figure 6. ESTARFM fusion results and 2D scatter plot of actual images.

3.2. Construction of Optimal Salinization Remote Sensing Monitoring Index Model

In order to ensure the objectivity of the feature variable selection and improve the inversion accuracy for salinization, this study adopted the random forest algorithm to

optimize the land-surface parameters that were derived from reconstructed time series (21a) TM images. Finally, the average importance scores of all the feature variables from the period 2000–2020 were obtained and ranked (Figure 7), and the feature variables with lower importance scores were removed. Using the 2D scatterplot tool in ENVI5.3, 12 feature spaces were constructed. Based on the spatial distribution law of the levels of soil salinization in the feature space, the feature space models could be divided into a point-to-point model and a point-to-line model (Figure 8).

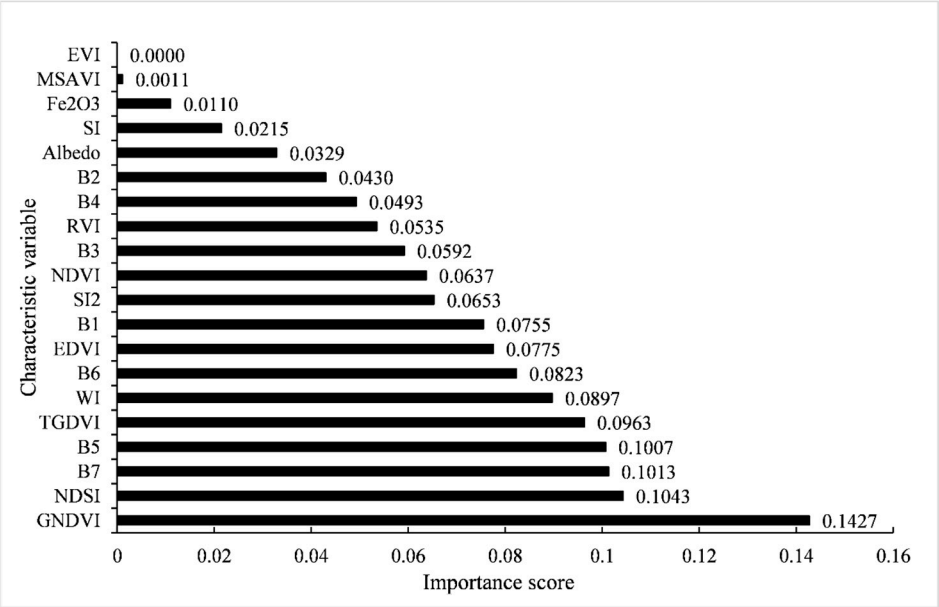


Figure 7. Optimization of salinization characterization parameters in the Yellow River Delta.

The construction of the NDSI-TGDVI feature space monitoring model based on point-to-point mode is shown in Figure 9. There was a certain nonlinear relationship between the normalized salinity index and the green normalized vegetation index, which was consistent with the trajectory of the soil salinization degree in the feature space. As the TGDVI increased, the NDSI gradually decreased based on the distance from any point M (X0, Y0) to point O (1,0) in the feature space: the greater the distance between M and O, the more severe the salinization; conversely, this led to a lower degree of salinization. Thus, L_1 was used to represent the distance between OMs to distinguish different degrees of salinization. Therefore, the NDSI-TGDVI monitoring index based on point-to-point mode was constructed as follows:

$$\mathrm{DMI1} = L_1 = \sqrt{\left(\mathrm{NDSI} - 1\right)^2 + \mathrm{TGDVI}^2} \quad (5)$$

The construction of the EDVI-Albedo feature space monitoring model based on point-to-line mode is shown in Figure 10. The nonlinear relationship between the extended difference vegetation index and surface albedo was highly significant, which was consistent with the trajectory of soil salinization in the feature space. As the EDVI increased, the surface albedo also gradually increased based on the distance from any point P (X0, Y0) to line L_1 in the feature space: the smaller the distance from point P to line L_1 was, the more severe the salinization was, and vice versa. Thus, L_2 was used to represent the distance between point P and L_1 to distinguish different degrees of salinization. Therefore, the EDVI-Albedo monitoring index based on point-to-line mode was constructed as follows:

$$\mathrm{DMI2} = L_2 = \frac{|0.7142\mathrm{EDVI} + \mathrm{Albedo} - (-0.1057)|}{\sqrt{1 + 0.7142^2}} \quad (6)$$

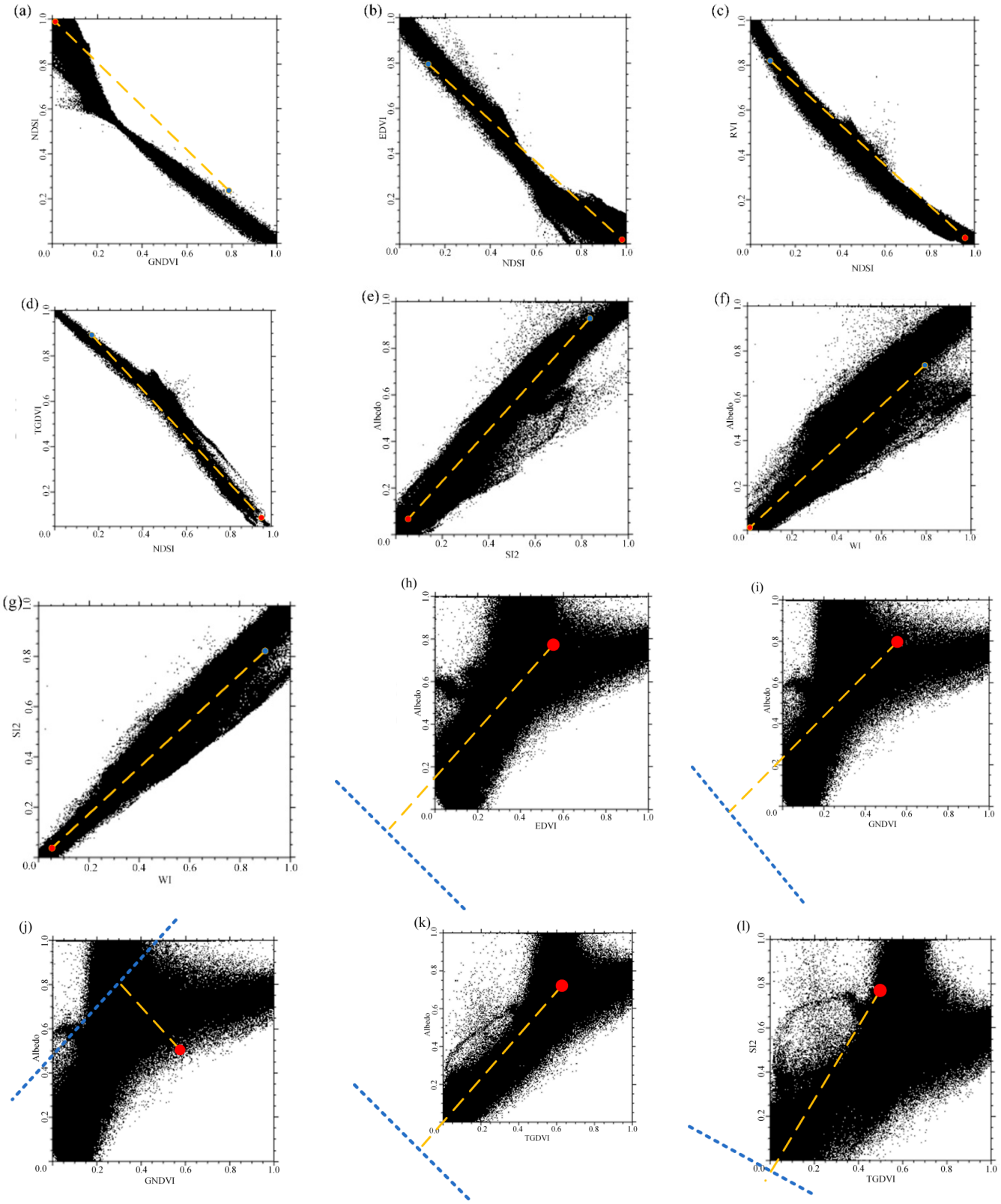


Figure 8. Characteristic space salinization monitoring indicator models: (**a**) GNDVI-NDSI; (**b**) NDSI-EDVI; (**c**) NDSI-RVI; (**d**) NDSI-TGDVI; (**e**) SI2-Albedo; (**f**) WI-Albedo; (**g**) WI-SI2; (**h**) EDVI-Albedo; (**i**) GNDVI-Albedo; (**j**) NDSI-Albedo; (**k**) TGDVI-Albedo; and (**l**) TGDVI-SI2.

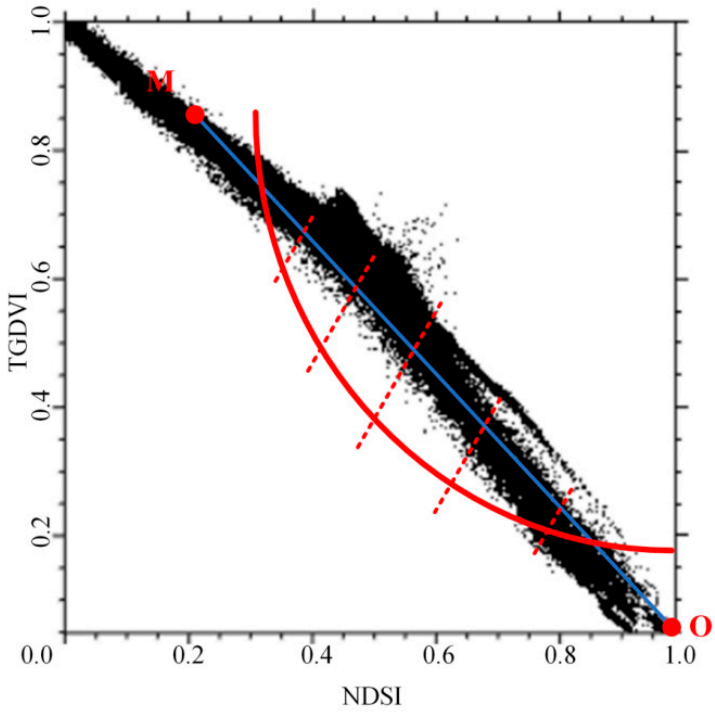


Figure 9. Construction of NDSI-TGDVI feature space salinization monitoring model based on point-to-point mode.

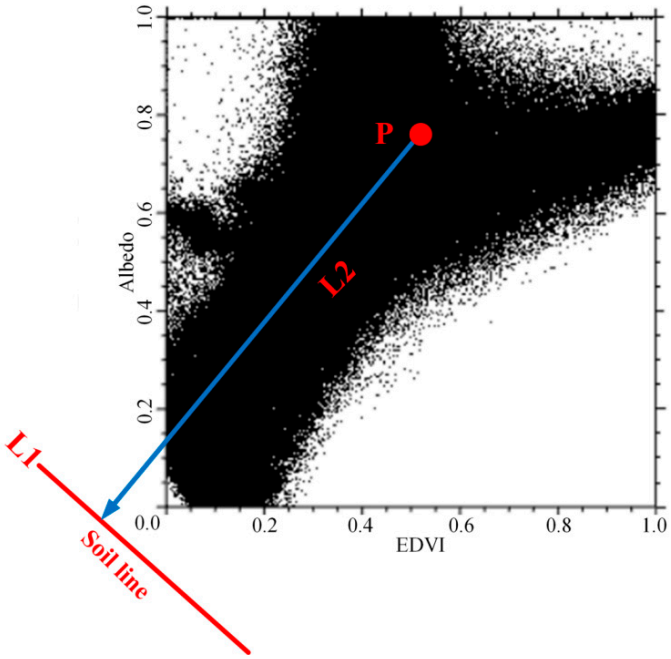


Figure 10. Construction of EDVI-Albedo feature space salinization monitoring model based on point-to-line mode.

In order to achieve better verification of the accuracy of the model and explore the applicability of different feature variables to the degree of salinization monitoring, this study selected 146 validation points from regions with different landscape types to compare and analyze the applicability of different feature space monitoring index models and then conducted a univariate linear regression analysis with the monitoring model values. At a significance level of <0.001, there were significant differences in the feature spaces constructed by different monitoring models. The corresponding formulas and accuracies

of the models are shown in Table 1: the optimal salinization monitoring index model was the NDSI-TGDVI monitoring index model using point-to-point mode, with R^2 = 0.9209, followed by the EDVI-Albedo monitoring index model using point-to-line mode, with R^2 = 0.9116.

Table 1. Comparison of levels of precision of different salinization monitoring index models.

Mode	Feature Space	Formula	R^2
point-to-point	GNDVI-NDSI	$DMI1 = L_1 = \sqrt{(GDVI-1)^2 + NDSI^2}$	0.8588
	NDSI-EDVI	$DMI2 = L_2 = \sqrt{(NDSI-1)^2 + EDVI^2}$	0.9007
	NDSI-RVI	$DMI3 = L_3 = \sqrt{(NDSI-1)^2 + RVI^2}$	0.873
	NDSI-TGDVI	$DMI4 = L_4 = \sqrt{(NDSI-1)^2 + TGDVI^2}$	0.9209
	SI2-Albedo	$DMI5 = L_5 = \sqrt{SI_2{}^2 + Albedo^2}$	0.5608
	WI-Albedo	$DMI6 = L_6 = \sqrt{WI^2 + Albedo^2}$	0.526
	WI-SI2	$DMI7 = L_7 = \sqrt{WI^2 + SI_2{}^2}$	0.627
point-to-line	EDVI-Albedo	$DMI8 = L_8 = \frac{\lvert 0.7142EDVI + Albedo - (-0.1057)\rvert}{\sqrt{1+0.7142^2}}$	0.9116
	GNDVI-Albedo	$DMI9 = L_9 = \frac{\lvert 0.7148GNDVI + Albedo - (-0.0935)\rvert}{\sqrt{1+0.7148^2}}$	0.6608
	NDSI-Albedo	$DMI10 = L_{10} = \frac{\lvert -0.5584NDSI + Albedo - 0.445\rvert}{\sqrt{1+(-0.5584)^2}}$	0.6944
	TGDVI-Albedo	$DMI11 = L_{11} = \frac{\lvert 0.6046TGDVI + Albedo - (-0.1142)\rvert}{\sqrt{1+0.6046^2}}$	0.7462
	TGDVI-SI_2	$DMI12 = L_{12} = \frac{\lvert 0.3394TGDVI + SI_2 - (-0.0887)\rvert}{\sqrt{1+0.3394^2}}$	0.607

3.3. Temporal Changes in Salinization Monitoring Models from 2000 to 2020

The annual salinization datasets from 2000 to 2020 were inversed using the NDSI-TGDVI feature space salinization monitoring index model based on point-to-point mode, and then the evolution patterns of soil salinization were analyzed. As shown in Figure 11, in the past 20 years, soil salinization in the Yellow River Delta region has shown an aggravation trend, and the average value reached its maximum in 2006 with 1.08. The minimum average value appeared in 2004, which was 0.393.

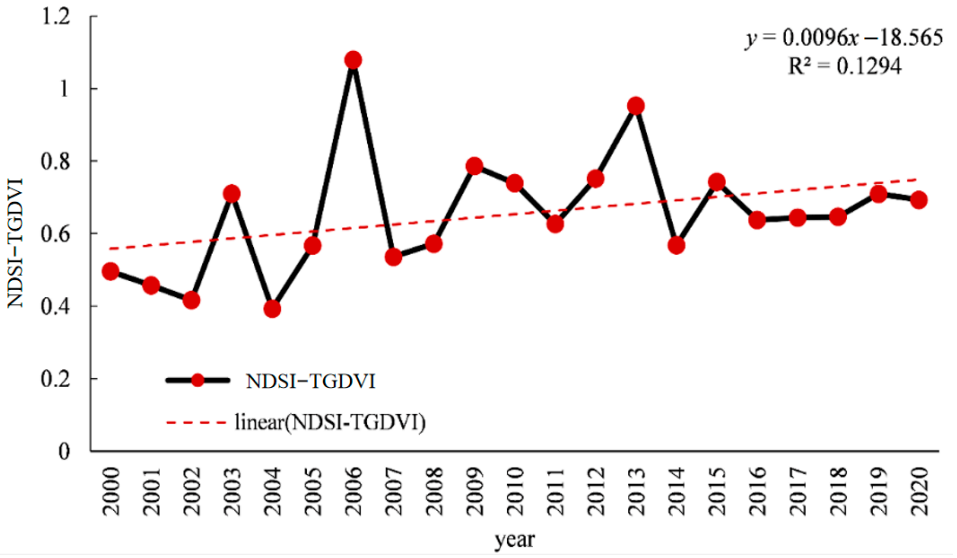


Figure 11. Temporal variations in average salinization monitoring model from 2000 to 2020.

3.4. Spatial Distribution Changes in Different Levels of Salinization from 2000 to 2020

In order to better reveal the spatial distribution of salinization, the levels of salinization were determined based on the natural breaks of ArcGIS 10.7 combined with the field-collected samples and the classification and grading standards for salinization: <0.2 was categorized as non-salinization, 0.2–0.4 as slight salinization, 0.4–0.6 as moderate salinization, 0.6–1.0 as severe salinization, and >1.0 as extreme salinization. As shown in Figure 12a, the total area of the Yellow River Delta in 2000 was 6624.93 km^2, and extreme- and moderate-salinization zones accounted for the smallest proportion, 4.2% and 3.9%, respectively, and were mainly distributed in coastal areas and the southeastern part of the Dongying District. Non-salinization and mild-salinization zones were mainly distributed in the southwestern parts of the study area, with a total area of 3259.6 km^2, accounting for about 50% of the entire study region. As shown in Figure 12b, compared with 2000, the area of the severe- and extreme-salinization zones increased significantly in 2005, reaching 1579.51 km^2. The area of the severe-salinization zones increased by 74%, which was mainly distributed in the coastal areas of the northern, eastern, and southeastern parts of the Yellow River Delta. Due to the large amount of water diversion and irrigation in the upper and middle reaches of the Yellow River Basin, the water volume in the lower reaches of the river decreased, leading to seawater intrusion and exacerbating the occurrence of salinization. The total area of the non-salinization and mild-salinization zones was 2556.6 km^2, with a decrease of 44%. As shown in Figure 12c, the area with extreme salinization significantly increased in 2010, which was mainly distributed in the northern and northeastern parts, the eastern coastal areas of the Kenli District, and the eastern coastal areas of the Dongying District. The area of the severe- and extreme-salinization zones was 1414.14 km^2, while that of the extreme-salinization zones accounted for 55%. The area of the slight-salinization zones increased significantly by 15% compared with 2000, while that of the moderate-salinization zones significantly decreased to 1568.13 km^2, representing a decrease of 44% compared with 2000. As shown in Figure 12d, the area of the severe- and extreme-salinization zones in 2015 was 2840.84, accounting for 43% of the total area, which was mainly distributed in the coastal areas of the Yellow River Delta. The area of the non-salinization and slight-salinization zones accounted for 23% compared with 2010, which were mainly distributed in the southwestern inland areas of the Yellow River Delta. As shown in Figure 12e, in 2020, most of the slight-salinization zones were transformed into moderate-salinization zones, with an area of 1523.83 km^2, accounting for 29%. The total area of the extreme- and severe-salinization zones was 2200.8 km^2, accounting for 33%, and its area proportion decreased by 10%. The area proportion of the non-salinization and slight-salinization zones increased by 21%, mainly distributed in the western part of Guangrao County, Lijin County, and the southern part of the Hekou District.

3.5. Migration Trajectory of Soil Salinization Gravity Center in the Yellow River Delta from 2000 to 2020

In order to better analyze the changes in the salinization gravity center in the Yellow River Delta over the past 20 years, this paper calculates and analyzes the mitigation trajectory of salinization at different timescales. As shown in Figure 13, in the past 20 years, the salinization gravity center has been located in the eastern part of Lijin County and adjacent to the Kenli District. Based on a 5-year timescale, the salinization gravity center first shifted 658.77 km to the northeast in 2000–2005, indicating that the soil salinization aggravation rate in the northeastern parts was significantly higher than that in the southwestern parts. From 2006 to 2010, the salinization gravity center slightly shifted 187.52 km to the northwest, indicating that the soil salinization aggravation rate in the northwestern parts was greater than that in the southeastern parts. From 2011 to 2015, the salinization gravity center migrated 2033 km to the southwest, and the migration distance was the largest, indicating that the aggravation rate of soil salinization in the southwestern parts was much higher than that in the northeastern parts during this period. From 2016 to 2020, the salinization gravity center shifted 5.57 km in the southeastern direction, indicating

that the soil salinization aggravation rate in the southeastern parts was higher than that in the northwestern parts during this period. Based on a 10-year scale, the salinization gravity center shifted 742.13 km to the northeastern region from 2000 to 2010, indicating that the aggravation rate of soil salinization was higher in the northeastern region than in the southwestern region. From 2011 to 2020, the gravity center shifted 1916.17 km to the southwestern region, and the migration distance was relatively large, indicating that the aggravation rate of salinization in the southwestern parts was much higher than that in the northeastern parts during this time period. At different timescales, the migration trajectory and distance pattern of salinization in the Yellow River Delta region were basically the same. Around 2010, the gravity center of soil salinization in the Yellow River Delta shifted towards the northeast, indicating that the aggravation degree and rate of salinization in the northeastern region were higher than those in the southwestern region. Around 2020, the gravity center of salinization shifted towards the southwest, indicating that the aggravation rate of salinization in the southwestern region was higher than that in the northeastern region. The salinization gravity centers were concentrated at the junction of the eastern part of Lijin County and Kenli County.

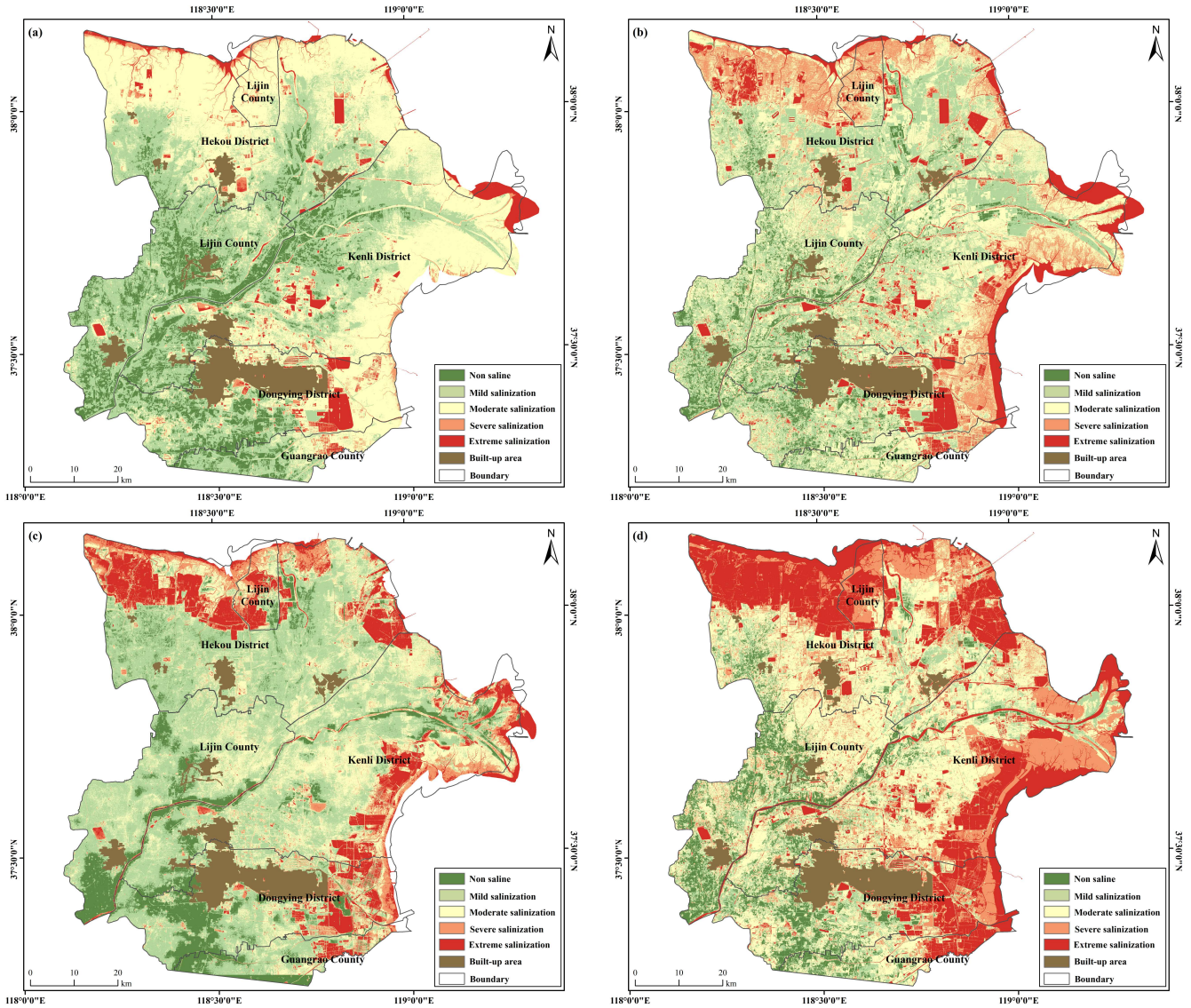


Figure 12. *Cont.*

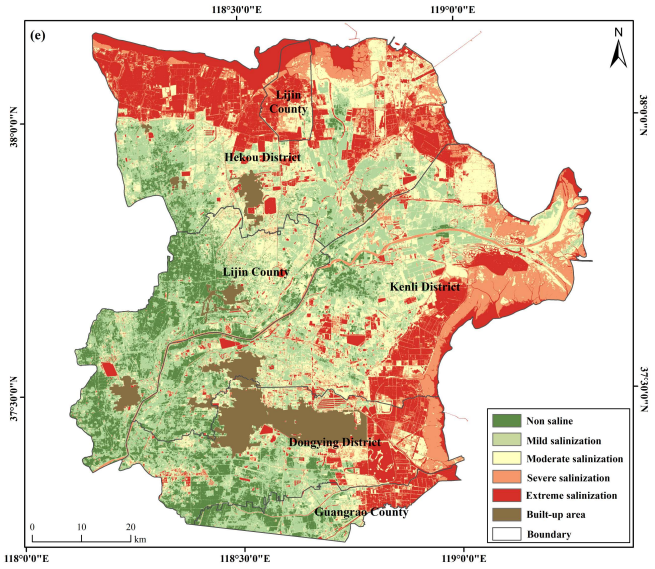


Figure 12. Spatial distribution of salinization at different levels: (**a**) 2000; (**b**) 2005; (**c**) 2010; (**d**) 2015; and (**e**) 2020.

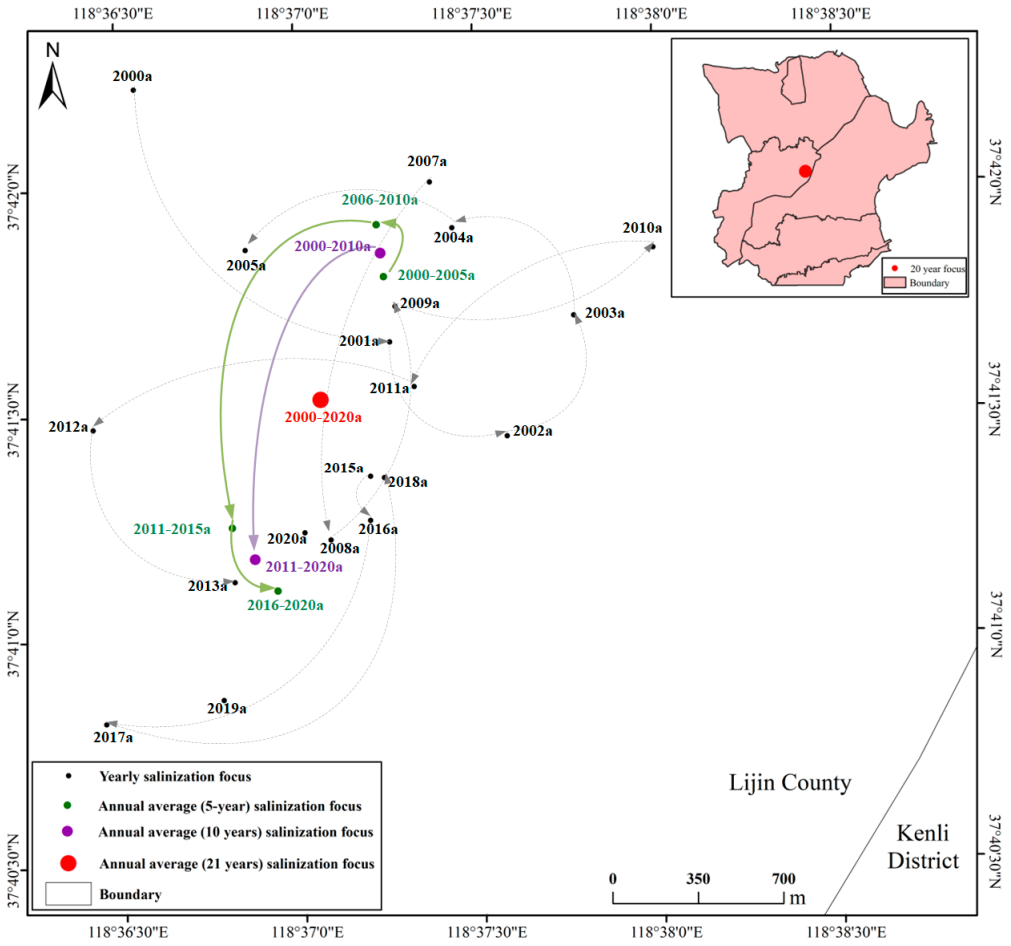


Figure 13. Migration trajectory of salinization gravity center in the Yellow River Delta at different timescales.

3.6. Dominant Driving Factor of Salinization Evolution

3.6.1. Dominant Single Factors in the Evolution of Salinization

There are certain differences in the dominant factors that affect the salinization evolution in the Yellow River Delta during different historical periods. In 2000, GDP had the largest q value at 0.68, indicating that human activity was the dominant factor affecting soil salinization in the region (Figure 14). In 2005, vegetation coverage had the greatest explanatory power for the evolution mechanism of salinization in the Yellow River Delta, with a q value of 0.71. In 2010, the maximum q value of precipitation was 0.78, indicating that precipitation had the greatest effect on the dissolution and release of soil salinity in the Yellow River Delta, followed by temperature. In 2015, the population had the largest q value at 0.65, followed by GDP with a q value of 0.43. In 2020, land use had the highest q value at 0.71, followed by soil moisture content at 0.69, indicating that the dominant factor affecting soil salinization in the region in 2020 was land use. The transformation between different types of land use can also affect soil salinization.

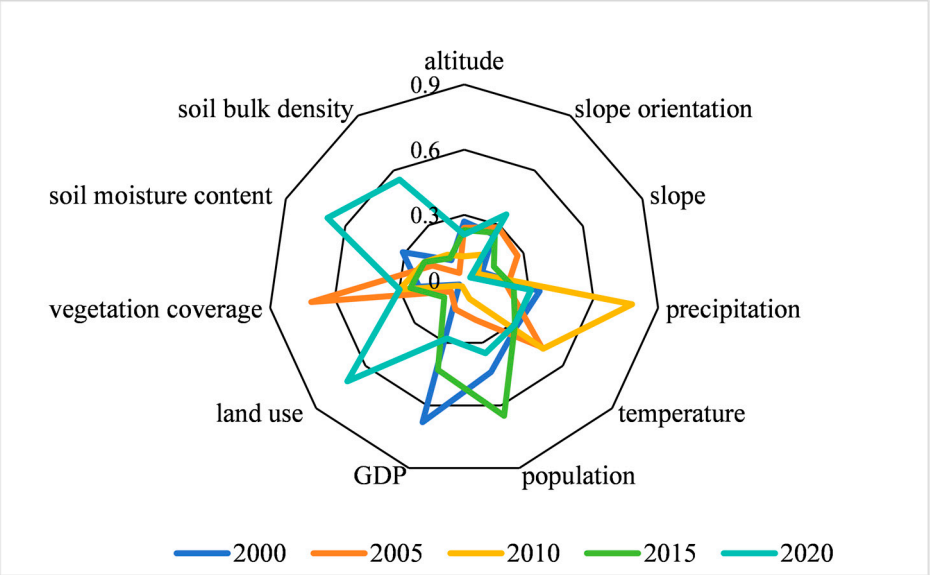


Figure 14. Q values of different driving factors in different years.

3.6.2. Dominant Interactive Factors in the Evolution of Salinization

Slope, precipitation, temperature, vegetation coverage, land use type, water content in the soil, and other driving factors had interactive effects on soil salinization, which changed in different historical periods. As shown in Figure 15, in 2000, the dominant interactive factors affecting soil salinization in the Yellow River Delta were precipitation ∩ slope direction (q = 0.96) and GDP ∩ temperature (q = 0.96), while in 2005, the dominant interactive factor was temperature ∩ slope direction (q = 0.97). The dominant interactive factors in 2010 were temperature ∩ slope direction (q = 0.92) and soil bulk density ∩ precipitation (q = 0.92). In 2015, the dominant interactive factors with the strongest explanatory power for the spatial differentiation of soil salinization were temperature ∩ slope direction (q = 0.94) and population ∩ temperature (q = 0.94). In 2020, the dominant interactive factors with the strongest explanatory power for the spatial differentiation of soil salinization were temperature ∩ slope direction (q = 0.84) and vegetation coverage ∩ precipitation (q = 0.84).

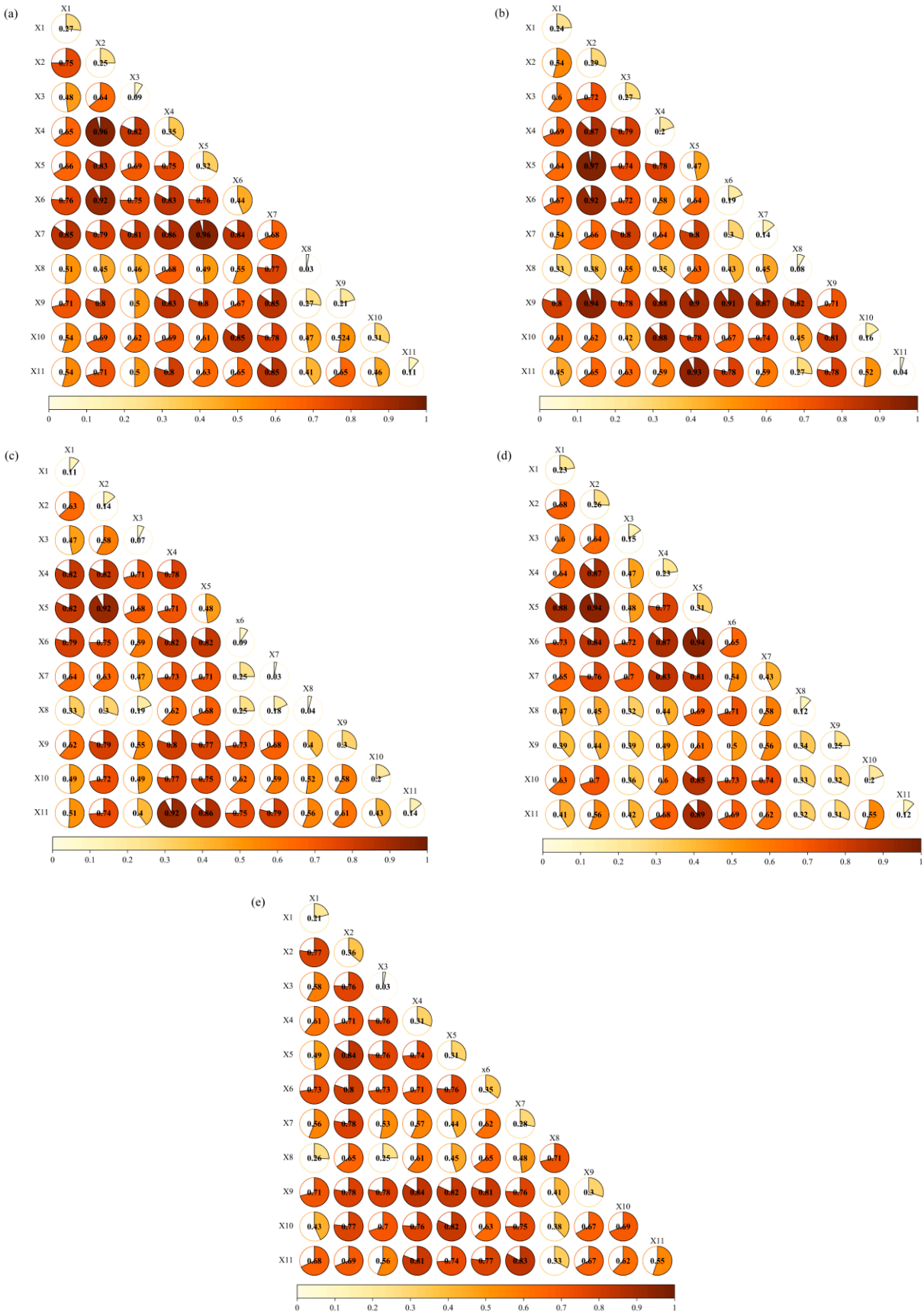


Figure 15. The dominant interactive factors of soil salinization in the Yellow River Delta. (**a**) 2000; (**b**) 2005; (**c**) 2010; (**d**) 2015; (**e**) 2020.

4. Discussion

4.1. Advantages of Research Model

The Yellow River Delta is located at the junction of the atmosphere, ocean, river, and land, with a typical interface of multiple ecological systems and a fragmented surface landscape pattern (especially wetlands), which lead to its intense environmental gradient and rapid salinization succession process [49]. Previous studies often utilized sparse time series or images from different seasons to conduct long-time-series studies, resulting in uncertainty in the inversion results for salinization [26]. This study obtained a dataset of long-time-series and similar phenological-fusion images in the study area based on the ESTARFM, which helped ensure the comparability and accuracy of salinization level estimations in our long-term analysis [28].

Previous studies have not considered the applicability and correlation of different parameters in determining the feature space parameters of salinization. This study utilized the random forest algorithm to effectively determine large-scale sensitive parameter sets, ranking the importance scores of different surface parameters, which led to the selection of 11 surface parameters with higher importance scores for soil salinization in the Yellow River Delta to construct feature spaces of different types. Random forest is an ensemble learning algorithm that improves overall accuracy by combining multiple decision trees and effectively processes surface parameters from different data sources, making it suitable for capturing complex, nonlinear relationships between surface parameters [50]. The accuracy of the TGDVI-NDS salinization remote sensing monitoring index model based on point-to-point mode was the highest. The reason was that the TGDVI was more sensitive to changes in the green band compared with the indices of vegetation types such as the NDVI and MSAVI [38]. Therefore, when evaluating the growth status of vegetation types, the TGDVI was more accurate compared with the NDSI [22]. The NDSI reduced the impacts of changes in different regions and at different times on the index itself, improved the stability and comparability of the index, and had higher sensitivity to different levels of salt, with a wider range of adaptability [15]. However, the salinization process was mostly influenced by multiple factors, meaning that the two-dimensional feature space model could not comprehensively reflect these interactive actions, and the n (>3) dimensional feature space model index should be constructed to improve the inversion accuracy.

4.2. Recent Causes of Soil Salinization Changes in the Yellow River Delta

From 2000 to 2020, due to differences in climate change, water resource management, land use and development, or other factors in different years, the degree of soil salinization in the Yellow River Delta fluctuated, and overall, it showed an increasing trend. In 2004, the average soil salinization was the lowest. According to a review of the Dongying government's work in 2004, the harmonious development of human activities and nature was coordinated, and the population, resources, and environmental work were strengthened, while farmland was protected, the land resource utilization efficiency was improved, and vegetation coverage increased by 4% [36]. A high vegetation coverage could help maintain soil stability and slow down water evaporation [26]. In 2006, the average soil salinization reached its maximum, and there was a significant decrease in precipitation in the Yellow River Delta region from 2000 to 2006 [51]. Due to insufficient precipitation, there was not enough water to leach the salt from the soil, resulting in the gradual accumulation of salt in the soil and an increase in salt concentration [23]. Additionally, the lack of precipitation could lead to a decline in the groundwater level, further causing the salt in the groundwater to rise to the soil surface and exacerbating the problem of soil salinization [29].

4.3. Analysis of the Driving Mechanism of Soil Salinization

Driving factors that are directly related to the bulk density and moisture content of soil, as well as land use, could directly reveal the degree of influence on salinization with relatively strong explanatory power. Factors such as vegetation coverage, precipitation, and temperature, which could directly affect soil moisture evaporation, also had relatively

strong explanatory power. The explanatory power of the spatial differentiation patterns of soil salinization was mostly enhanced by the dual factors, which included their own dominant factors, and the q values of most of the interactive dominant factors were greater than those of their respective driving factors. The explanatory power of the interactive factors was greater than that of single factors, indicating that soil salinization is not directly caused by a single driving factor but by the joint effects of all the driving factors [33]. The dominant factor affecting soil salinization in 2000 was GDP. Due to the location of the Yellow River Delta in Dongying City, the GDP growth rate of Dongying City reached 9.2% in 2000. The increase in GDP and the continuous improvement in the economic development level led to the unreasonable development and production of natural resources in the region, resulting in a decrease in land productivity and an increase in land vulnerability [32]. The waste of water resources and unreasonable irrigation led to seawater backflow, exacerbating soil salinization in the Yellow River Delta region [28]. The dominant factor in 2005 was vegetation coverage, which was part of the harmonious coordination of human development and nature. It strengthened population, resource, and environmental work, protected farmland, and improved the efficiency of land resource utilization. The dominant factor in 2010 was precipitation. The annual precipitation in the Yellow River Delta region in 2010 was 509.6 mm, and the fluctuations in annual precipitation in the years before and after 2010 were small and relatively stable. The dominant factor in 2015 was population, and the GDP of the Yellow River Delta region was on an increasing trend from 2000 to 2010. With the increase in population, the use of natural resources has intensified, thereby affecting the degree of soil salinization in the Yellow River Delta region [11]. In 2020, the dominant single factor was land use, with transitions between different land use types, such as the conversion from low-coverage grassland to high-coverage grassland, or the expansion of salt factories, also affecting soil salinization [44]. Regarding the dominant interactive factors in 2000, the dominant interactive factors were precipitation ∩ slope orientation and GDP ∩ slope orientation, while in 2005, the dominant interactive factor was temperature ∩ slope orientation. In 2010, the dominant interactive factors were temperature ∩ slope orientation and soil bulk density ∩ precipitation, while in 2015, the dominant interactive factors were temperature ∩ slope orientation and population ∩ temperature. In 2020, the dominant interactive factors were temperature ∩ slope orientation and vegetation coverage ∩ precipitation. The effects of temperature and slope orientation on soil salinization in the Yellow River Delta were intertwined and run through the entire study period. Slope orientation was an important factor on the surface of land, and different slope orientations might lead to differences in water distribution, soil erosion, vegetation coverage, and other aspects, thereby affecting the distribution and accumulation of salt in the soil [20]. A sunny slope is usually more susceptible to direct sunlight, which leads to intense water evaporation. A shady slope is relatively humid, which might result in more lush vegetation on the shady slope compared with the sunny slope, leading to more concentration of soil salt on the sunny slope and exacerbating salt accumulation [52]. Temperature was an important climate factor that affected soil salinization. High temperatures usually led to an increase in soil moisture evaporation, as well as an increase in vegetation transpiration, causing more water to evaporate from the soil [2]. When water evaporated, the salt in the soil gradually concentrated, resulting in water evaporation, while the salt remained in the soil.

5. Conclusions

Based on long-time-series and similar phenological-fusion images and utilizing the random forest algorithm, the surface parameters of salinization were optimized and, then, feature space index models were constructed. Combined with the measured ground data, the optimal monitoring index model of salinization was determined, and the spatiotemporal evolution patterns of salinization and its driving mechanisms in the Yellow River Delta were revealed. The research results are as follows:

(1) The result of the ESTARFM has the highest correlation coefficient, $R^2 = 0.8677$, indicating that the ESTARFM algorithm has better application in the Yellow River delta.

(2) The NDSI-TGDVI feature space salinization monitoring index model based on point-to-point mode has the highest accuracy of 0.92, followed by the EDVI-Albedo feature space salinization monitoring index model based on point-to-point mode, with an accuracy of 0.91.
(3) From 2000 to 2020, the remote sensing monitoring index model of soil salinization in the Yellow River Delta region showed an overall aggravation trend. The average salinization in the past 20 years was 0.65, which is categorized as severe salinization, and the degree of salinization gradually decreased from the northeastern coastal area to the southwestern inland area.
(4) The dominant factors affecting soil salinization vary in different historical periods, with little difference in the dominant interactive factors, which are mainly temperature and slope orientation.

Author Contributions: Conceptualization, methodology, and writing—original draft preparation, B.G.; investigation, supervision, project administration, and funding acquisition, M.X. and R.Z. All authors have read and agreed to the published version of the manuscript.

Funding: This research was funded by the National Natural Science Foundation of China (grant numbers: 42471329, 42101306, 42301102), Scientific Innovation Project for Young Scientists in Shandong Provincial Universities (grant number: 2022KJ224), the Natural Science Foundation of Shandong Province (grant number: ZR2021MD047), and the Gansu Youth Science and Technology Fund Program (grant numbers: 24JRRA100).

Data Availability Statement: Data are contained within the article.

Conflicts of Interest: The authors declare no conflicts of interest.

Appendix A

Table A1. List of Landsat and MODIS image information.

Code	Time of Fine-Resolution Image	Type of Fine-Resolution Image	Resolution	Type of Coarse-Resolution Image	Time of Coarse-Resolution Image	Time of Fusion Image	Resolution	Time of Reconstructed Images
1	8 April 2000	TM	30	--	--	--	--	8 April 2000
2	10 March 2001	TM	30	MOD09A1	6 March 2001	15 April 2001	500	15 April 2001
	16 July 2001	TM	30		12 July 2001		500	
3	8 January 2002	TM	30	MOD09A1	9 January 2002	15 April 2002	500	15 April 2002
	7 October 2002	TM	30		8 October 2002		500	
4	12 February 2003	TM	30	MOD09A1	10 February 2003	15 April 2003	500	15 April 2003
	20 June 2003	TM	30		18 June 2003		500	
5	19 April 2004	TM	30	--	--	--	--	19 April 2004
6	22 April 2005	TM	30	--	--	--	--	22 April 2005
7	9 April 2006	TM	30	--	--	--	--	9 April 2006
8	11 March 2007	TM	30	MOD09A1	14 March 2007	15 April 2007	500	15 April 2007
	14 May 2007	TM	30		17 May 2007		500	
9	14 April 2008	TM	30	--	--	--	--	14 April 2008
10	1 April 2009	TM	30	--	--	--	--	1 April 2009
11	11 September 2010	TM	30	MOD09A1	14 September 2010	15 April 2010	500	15 April 2010
	14 January 2010	TM	30		17 January 2010		500	
12	22 March 2011	TM	30	MOD09A1	22 March 2011	15 April 2011	500	15 April 2011
	2 February 2011	TM	30		2 February 2011		500	
13	17 April 2012	ETM+	30	--	--	--	--	17 April 2012
14	30 May 2013	OLI	30	MOD09A1	25 May 2013	15 April 2013	500	15 April 2013
	30 May 2013	OLI	30		17 May 2013		500	

Table A1. *Cont.*

Code	Time of Fine-Resolution Image	Type of Fine-Resolution Image	Resolution	Type of Coarse-Resolution Image	Time of Coarse-Resolution Image	Time of Fusion Image	Resolution	Time of Reconstructed Images
15	14 March 2014	OLI	30	MOD09A1	14 March 2014	15 April 2014	500	15 April 2014
	1 May 2014	OLI	30		1 May 2014		500	
16	1 March 2015	OLI	30	MOD09A1	6 March 2015	15 April 2010	500	15 April 2015
	4 May 2015	OLI	30		01 May 2015		500	
17	3 March 2016	OLI	30	MOD09A1	5 March 2016	14 April 2016	500	14 April 2016
	19 March 2016	OLI	30		21 March 2016		500	
18	23 April 2017	OLI	30	--	--	--	--	23 April 2017
19	25 March 2018	OLI	30	MOD09A1	22 March 2018	15 April 2018	500	15 April 2018
	9 March 2018	OLI	30		3 March 2018		500	
20	12 March 2019	OLI	30	MOD09A1	14 March 2019	15 April 2019	500	15 April 2019
	23 January 2019	OLI	30		25 January 2019		500	
21	15 April 2020	OLI	30	--	--	--	--	15 April 2020

References

1. Zhao, M.; Chang, C.Y.; Wang, Z.R.; Zhao, G.X. Driving Force Analysis and Prediction Simulation of Soil Salinization in Coastal Area of Yellow River Delta. *Chin. Agric. Sci. Bull.* **2024**, *40*, 75–83.
2. Zhang, S.N.; Lu, M.; Wen, C.Y.; Song, Y.Q.; Kang, L.; Shen, J.H.; Yang, M.Z. Study of soil salinity remote sensing inversion method integrating crop type. *Bull. Surv. Mapp.* **2024**, *2*, 1–7.
3. Zhang, Z.M.; Fan, Y.G.; Jiao, Z.J.; Guan, Q.C. Impact of salinization on the eco-environment quality of coastal wetlands; A case study of Yellow River Delta. *Remote Sens. Nat. Resour.* **2023**, *35*, 226–235.
4. Fan, X.M.; Liu, G.H.; Liu, H.G. Yellow River Delta based on Kriging and Cokriging methods Evaluation of soil salinization. *Resour. Sci.* **2014**, *36*, 321–327.
5. Zhang, Z.T.; Wei, G.F.; Yao, Z.H.; Tan, C.X.; Wang, X.T.; Han, J. Soil Salt Inversion Model Based on UAV Multispectral Remote Sensing. *Tran. Chin. Soc. Agric. Mach.* **2019**, *50*, 151–160.
6. Wang, J.Q.; Peng, J.; Li, H.Y.; Yin, C.Y.; Liu, W.Y.; Wang, T.W.; Zhang, H.P. Soil salinity mapping using machine learning algorithms with the Sentinel-2 MSI in arid areas, China. *Remote Sens.* **2021**, *13*, 305. [CrossRef]
7. Liu, Y.; Pan, X.Z.; Shi, R.J.; Li, Y.L.; Wang, C.K.; Li, Z.T. Estimation of Soil Salt Content over Partially Vegetated Areas Based on Blind Source Separation. *Acta Pedo Sinica* **2016**, *53*, 322–331.
8. Li, J.H.; Gao, M.X. Temporal and Spatial Characteristics of Salinization of Coastal Soils in the Yellow River Delta. *Chin. J. Soil Sci.* **2018**, *49*, 1458–1465.
9. Singh, A. Soil salinization management for sustainable development: A review. *J. Environ. Manag.* **2021**, *277*, 111383. [CrossRef]
10. Yang, J.S.; Yao, R.J.; Wang, X.P.; Xie, W.P.; Zhang, X.; Zhu, W.; Zhang, L.; Sun, R.J. Research on Salt-affected Soils in China: History, Status Quo and Prospect. *Acta Pedo Sinica* **2022**, *59*, 10–27.
11. Wang, D.Y.; Chen, H.Y.; Wang, G.F.; Cong, J.Q.; Wang, X.F.; Wei, X.W. Salinity Inversion of Severe Saline Soil in the Yellow River Estuary Based on UAV Multi-Spectra. *Sci. Agric. Sinica* **2019**, *52*, 1698–1709.
12. Shi, H.B.; Wu, D.; Yan, J.W.; Li, X.Y.; Zhu, K.; Chi, B.X. Spatial-temporal Variation of Soil Salinity after Water Saving Transformation in Salinized Irrigation District. *Tran. Chin. Soc. Agric. Mach.* **2020**, *51*, 318–331.
13. Wang, F.; Ding, J.L. Soil Salinity Modelling Study with Salinity Inference Model Based on the Integration of Soil and Vegetation Spectrum in Arid Land. *Spect. Spect. Anal.* **2016**, *36*, 1848–1853.
14. Zhang, T.J.; Chen, Y.J.; Liu, J.Z. Characteristics of soil salinization in coastal wetlands based on canonical correspondence analysis. *Acta Ecol. Sinica* **2019**, *39*, 3322–3332.
15. Chen, X.L.; Wang, Y.F.; Zhang, H.M.; Liu, F.G.; Shen, Y.J. Extraction method of irrigated arable land in the Chahannur Basin based on the ESTARFM NDVI. *Chin. J. Eco-Agric.* **2021**, *29*, 1105–1116.
16. Yang, L.B.; Chen, C.B.; Zheng, H.W.; Luo, G.P.; Shang, B.J.; Olaf, H. Retrieval of Soil Salinity Content based on Random Forests Regression Optimized by Bayesian Optimization Algorithm and Genetic Algorithm. *J. Geo-Inf. Sci.* **2021**, *23*, 1662–1674.
17. Kumar, P.; Tiwari, P.; Biswas, A.; Srivastava, P.K. Spatio-temporal assessment of soil salinization utilizing remote sensing derivatives, and prediction modeling: Implications for sustainable development. *Geosci. Front.* **2024**, *15*, 101881. [CrossRef]
18. Wang, N.; Chen, S.; Huang, J.; Frappart, F.; Taghizadeh, R.; Zhang, X.; Wigneron, J.; Xue, J.; Xiao, Y.; Peng, J.; et al. Global Soil Salinity Estimation at 10 m Using Multi-Source Remote Sensing. *J. Remote Sens.* **2024**, *4*, 0130. [CrossRef]
19. Alaa, A.M.; Katsuaki, K.; Mohames, M.-E.-H.; Khaled, S.G. Mapping soil salinity using spectral mixture analysis of Landsat 8 OLI images to identify factors influencing salinization in an arid region. *Int. J. Appl. Earth Obs.* **2019**, *83*, 101944.

20. Zhuang, Q.W.; Shao, Z.F.; Huang, X.; Zhang, Y.; Wu, W.F.; Feng, X.X.; Lv, X.W.; Ding, Q.; Cai, B.W.; Altan, O. Evolution of soil salinization under the background of landscape patterns in the irrigated northern slopes of Tianshan Mountains, Xinjiang, China. *Catena* **2021**, *206*, 105561. [CrossRef]
21. Wang, Z.; Zhang, F.; Zhang, X.L.; Chan, N.W.; Kung, H.T.; Ariken, M.; Zhou, X.H.; Wang, Y.S. Regional suitability prediction of soil salinization based on remote-sensing derivatives and optimal spectral index. *Sci. Total Environ.* **2021**, *775*, 145807. [CrossRef] [PubMed]
22. Ding, J.L.; Yao, Y.; Wang, F. Detecting soil salinization in arid regions using spectral feature space derived from remote sensing data. *Acta Ecol. Sin.* **2014**, *34*, 4620–4631.
23. Guo, B.; Zang, W.Q.; Han, B.M.; Yang, F.; Luo, W.; He, T.L.; Fan, Y.W.; Yang, X.; Chen, S.T. Dynamic monitoring of desertification in Naiman Banner based on feature space models with typical surface parameters derived from Landsat images. *Land. Degrad. Dev.* **2020**, *31*, 1573–1592. [CrossRef]
24. Shoba, P.; Kokila, P.R. A novel approach to quantify soil salinity by simulating the dielectric loss of SAR in three-dimensional density space. *Remote Sens. Eniron.* **2020**, *251*, 112059.
25. Zhang, T.Y.; Wang, L.; Zeng, P.L.; Wang, T.; Geng, Y.H.; Wang, H. Soil Salinization in the Irrigated Area of the Manas River Basin Based on MSAVI-SI Feature Space. *Arid. Zone Res.* **2016**, *33*, 499–505.
26. Guo, B.; Yang, F.; Han, B.M.; Fan, Y.W.; Chen, S.T.; Yang, W.N.; Jiang, L. A model for the rapid monitoring of soil salinization in the Yellow River Delta using Landsat 8 OLI imagery based on VI-SI feature space. *Remote Sens. Lett.* **2019**, *10*, 796–805. [CrossRef]
27. Bian, L.L.; Wang, J.L.; Liu, J.; Han, B.M. Spatiotemporal changes of soil salinization in the Yellow River Delta of China from 2015 to 2019. *Sustainability* **2021**, *13*, 822. [CrossRef]
28. Wu, Z.H.; Yan, Q.W.; Zhang, S.T.; Lei, S.G.; Lu, Q.Q.; Hua, X. Remote sensing monitoring of soil salinization based on SI-Brightness feature space and drivers analysis: A case study of surface mining areas in semi-arid steppe. *IEEE Access* **2021**, *9*, 110137–110148. [CrossRef]
29. Guo, B.; Zang, W.Q.; Luo, W.; Wen, Y.; Yang, F.; Han, B.M.; Fan, Y.W.; Chen, X.; Qi, Z.; Wang, Z. Detection model of soil salinization information in the Yellow River Delta based on feature space models with typical surface parameters derived from Landsat8 OLI image. *Geomat. Nat. Hazards Risk* **2020**, *11*, 288–300. [CrossRef]
30. Yao, Y.; Ding, J.L.; Wang, S. Soil salinization monitoring in the Werigan-Kuqa Oasis, China, based on a three-dimensional feature space model with machine learning algorithm. *Remote Sens. Lett.* **2021**, *12*, 269–277. [CrossRef]
31. Guo, B.; Liu, Y.F.; Fan, J.F.; Lu, M.; Zang, W.Q.; Liu, C.; Wang, B.Y.; Huang, X.Z.; Lai, J.B.; Wu, H.W. The salinization process and its response to the combined processes of climate change–human activity in the Yellow River Delta between 1984 and 2022. *Catena* **2023**, *231*, 107301. [CrossRef]
32. Wang, F.; Yang, S.T.; Wei, Y.; Shi, Q.; Ding, J.L. Characterizing soil salinity at multiple depth using electromagnetic induction and remote sensing data with random forests: A case study in Tarim River Basin of southern Xinjiang, China. *Sci. Total Environ.* **2020**, *754*, 142030. [CrossRef] [PubMed]
33. Huang, C.; Zhang, C.C.; Liu, Q.S.; Li, H.; Yang, X.M.; Liu, G.H. Multi-Feature Classification of Optical and SAR Remote Sensing Images for Typical Tropical Plantation Species. *Sci. Silvae Sin.* **2021**, *57*, 80–91.
34. Yang, X.H.; Luo, Y.Q.; Yang, H.C.; Zhang, F.H.; Lei, J.J. Soil salinity retrieval and spatial distribution of oasis farmland in Manasi river basin. *J. Arid. Land. Resour. Environ.* **2021**, *35*, 156–161.
35. Wu, C.S.; Huang, C.; Liu, G.H.; Liu, Q.S. Assessment of ecological vulnerability in the Yellow River Delta using the Fuzzy Analytic Hierarchy Process. *Acta Ecol. Sin.* **2018**, *38*, 4584–4595.
36. Guo, B.; Yang, F.; Fan, Y.W.; Han, B.M.; Chen, S.T.; Yang, W.N. Dynamic monitoring of soil salinization in Yellow River Delta utilizing MSAVI–SI feature space models with Landsat images. *Environ. Earth Sci.* **2019**, *78*, 308. [CrossRef]
37. Huang, B.; Zhao, Y.Q. Research Status and Prospect of Spatiotemporal Fusion of Multi-source Satellite Remote Sensing Imagery. Acta. *Geoda Carto Sin.* **2017**, *46*, 1492–1499.
38. Chen, H.Y.; Ma, Y.; Zhu, A.X.; Wang, Z.R.; Zhao, G.X.; Wei, Y.N. Soil salinity inversion based on differentiated fusion of satellite image and ground spectra. *Int. J. Appl. Earth Obs.* **2021**, *101*, 102360. [CrossRef]
39. Wu, Z.J.; Zhang, J.H.; Deng, F.; Zhang, S.; Zhang, D.; Xun, L.; Javed, T.; Liu, G.Z.; Liu, D.; Ji, M.F. Fusion of GF and MODIS data for regional-scale grassland community classification with EVI2 time-series and phenological features. *Remote Sens.* **2021**, *13*, 835. [CrossRef]
40. Liu, M.L.; Ke, Y.H.; Yin, Q.; Chen, X.W.; Im, J.H. Comparison of five spatio-temporal satellite image fusion models over landscapes with various spatial heterogeneity and temporal variation. *Remote Sens.* **2019**, *11*, 2612. [CrossRef]
41. Ping, B.; Meng, Y.S.; Su, F.Z. Comparisons of Spatio-temporal Fusion Methods for GF-1 WFV and MODIS Data. *J. Geo-Inf. Sci.* **2019**, *21*, 157–167.
42. Alonso, A.; Munoz-Carpena, R.; Kaplan, D. Coupling high-resolution field monitoring and MODIS for reconstructing wetland historical hydroperiod at a high temporal frequency. *Remote Sens. Environ.* **2020**, *247*, 111807. [CrossRef]
43. Januar, T.W.; Lin, T.H.; Huang, C.Y.; Chang, K.E. Modifying an image fusion approach for high spatiotemporal LST retrieval in surface dryness and evapotranspiration estimations. *Remote Sens.* **2020**, *12*, 498. [CrossRef]
44. Yan, Y.C.; Wu, C.J.; Wen, Y.Y. Determining the impacts of climate change and urban expansion on net primary productivity using the spatio-temporal fusion of remote sensing data. *Ecol. Indic.* **2021**, *127*, 107737. [CrossRef]

45. Jiang, D.P.; Du, J.; Song, K.S.; Zhao, B.Y.; Zhang, Y.W.; Zhang, W.J. Classification of Conservation Tillage Using Enhanced Spatial and Temporal Adaptive Reflectance Fusion Model. *Remote Sens.* **2023**, *15*, 508. [CrossRef]
46. Leo, B. Random Forests. *Mach. Learn.* **2001**, *45*, 5–32.
47. Bi, S.B.; Ji, H.; Chen, C.C.; Yang, H.R.; Shen, X. Application of geographical detector in human-environment relationship study of prehistoric settlements. *Prog. Geogra* **2015**, *34*, 118–127.
48. Yang, Y.H. Spatial and Temporal Fusion of Evapotranspiration Based on Multi-source Remote Sensing Data: A case study of Houzhai River sub-basin in Guizhou Province. *Sci. Technol. Indus* **2023**, *23*, 236–244.
49. Xie, C.H.; Zhang, S.Y.; Cui, L.Z.; An, W.T.; Tang, J.K. Progress and Trend of Remote Sensing Classification of Land Cover in the Yellow River Delta. *Sci. Technol. Eng.* **2022**, *42*, 4524–4535.
50. Wang, X.N.; Su, W.H.; Dong, L.B. Age estimation model for individual tree in natural Larix gmelinii forest based on random forest. *Chin. J. Appl. Ecol.* **2024**, *5*, 1055–1063.
51. Cao, Y.; Sun, Y.L.; Chen, Z.X.; Yan, H.; Qian, S. Dynamic changes of vegetation ecological quality in the Yellow River Basin and its response to extreme climate during 2000-2020. *Acta Ecol. Sin.* **2022**, *42*, 4524–4535.
52. Xu, C.D.; Wang, R.R.; Cheng, H.; Lian, H.D.; Gong, X.W.; Liu, L.Y.; Wang, Y. Spatial-temporal distribution of water and salt in artificial oasis irrigation area in arid area based on remote sensing analysis. *Trans. CSAE* **2019**, *35*, 80–89.

Disclaimer/Publisher's Note: The statements, opinions and data contained in all publications are solely those of the individual author(s) and contributor(s) and not of MDPI and/or the editor(s). MDPI and/or the editor(s) disclaim responsibility for any injury to people or property resulting from any ideas, methods, instructions or products referred to in the content.